

VIP Very Important Paper

# General Synthesis of Heteroatom-Doped Hierarchical Carbon toward Excellent Electrochemical Energy Storage

Guoqiang Zou,<sup>[a]</sup> Hongshuai Hou,\*<sup>[a]</sup> Jiugang Hu,<sup>[a]</sup> and Xiaobo Ji<sup>[a]</sup>

Heteroatom-doping is an effective approach to modify the microstructure of carbon-based materials toward enhanced electrochemical energy storage performance. Nevertheless, it is a great challenge to obtain a specific heteroatom-doped carbon material with hierarchical structure as a general doping strategy is missing. Herein, carbon materials doped with P, S and both of them are designed and precisely prepared through in-situ polymerization. Used as anode for sodium-ion batteries, the best performing material displays a high specific capacity of  $368.6 \text{ mAh g}^{-1}$  at a current density of  $0.1 \text{ A g}^{-1}$  after 100 cycles. A high capacity of  $159.8 \text{ mAh g}^{-1}$  is achieved at a large current

density of  $5 \text{ A g}^{-1}$ . Impressively, this material also delivers robust storage performances for lithium. According to the first-principles method and detailed experimental data, the expanded interlayer distance and enhanced electronic conductivity of the microcrystalline region can be attributed to C–S and P–C bonds, while the high surface capacitance contribution can be assigned to surface C–S species and highly exposed edges of the microcrystalline region. This work sheds light on a promising method for the exploitation of versatile heteroatom modified hierarchical carbon materials.

## 1. Introduction

In recent decades, carbon materials with different micro/nano-structures and dimensions have been widely applied in catalysis,<sup>[1]</sup> separation/adsorption,<sup>[2]</sup> biosensors,<sup>[3]</sup> and energy storage<sup>[4]</sup> due to their large specific surface areas, regulatable pore structure, good thermal stability and electronic conductivity. For instance, the carbon nanotubes (CNTs) with 1D tubular structure receive huge attention in many areas of science and engineering thanks to their unique chemical properties.<sup>[2a,3]</sup> In addition, carbon nanowire,<sup>[4a]</sup> graphene,<sup>[5]</sup> carbon nanosheets,<sup>[6]</sup> and 3D carbon micro/nano-spheres<sup>[7]</sup> were also fabricated. Among them, 3D carbon materials have been received lots of notice in many fields by reason of their fast mass transfer processes. Phosphorus-doped 3D hierarchical porous carbons were prepared through the carbonization of mixture composing of glucose, manganese nitrate and sodium hypophosphite, showing an excellent specific capacitance of  $367 \text{ F g}^{-1}$  at  $0.3 \text{ A g}^{-1}$ .<sup>[8]</sup> To further ameliorate performances, a 3D bubble-like porous carbon were designed by Shen et al., delivering a high catalytic activity for the direct oxidation of benzene to phenol.<sup>[9]</sup> Lately, Wang et al. developed a nitrogen and sulfur dual-doped hierarchical bubble-like carbon (NSHPC) by employing the lotus plumulea as carbon sources. When was utilized as carrier for sulfur in lithium-sulfur batteries, a high first discharge capacity of  $1549 \text{ mAh g}^{-1}$  can be acquired at  $0.1 \text{ C}$ .<sup>[10]</sup> To date, some developments have been obtained for the fabrication of

bubble-like carbon, however, a low cost and simple method for the preparation of the unique carbon materials are still urgently desired.

The fast exhaustion of nonrenewable fossil resources and increasing worries about global environmental issues facilitate the advance of cleaner energy sources. Nonetheless, merging discontinuous cleaner energy sources into the state grid are also full of challenge.<sup>[11]</sup> Sodium ion secondary batteries (SIBs) are regarded as a great prospective equipment to integrate these sporadic energies on account of their abundant sources, cheap price and low maintenance cost.<sup>[11b,12]</sup> However, the development of high performance anode materials for SIBs remains a challenge as a result of the larger ionic radius of the sodium ion compared than that of lithium ion, bringing sluggish diffusion kinetics processes.<sup>[13]</sup> Drawing on the great success of graphite as anode for lithium ion batteries (LIBs), carbon materials are deemed as one of the most promising anodes for SIBs. Since the sodium ions are difficult to be embedded into layers of graphite with small interlayer space, amorphous carbons with a large number of microcrystalline regions are considered to be a better electrode material for SIBs. For example, an amorphous hollow carbon nanowire was obtained by the direct pyrolysis of a hollow polyaniline, presenting a capacity of  $149 \text{ mAh g}^{-1}$  at  $0.5 \text{ A g}^{-1}$ .<sup>[4a]</sup> Our group reported a new 3D porous carbon obtained from carbon quantum dots, delivering a remarkable electrochemical performances.<sup>[14]</sup> Recently, lots of research outcomes indicate that the doping of heteroatoms (N, S or P) can efficiently expand the interlayer spacing and simultaneously enhance the electronic conductivity of the carbon materials.<sup>[4d,6a,15]</sup> A sulfur-doped carbon with enlarged interlayer distance has been prepared by Huang et al. and showed a high reversible capacity of  $242 \text{ mAh g}^{-1}$  at  $1 \text{ A g}^{-1}$ .<sup>[16]</sup> Although sulfur-doping can effectively enhance the electrochemical performance of the carbon materials, however, a high doping of sulfur will enhance

[a] Prof. G. Zou, H. Hou, Prof. J. Hu, Prof. X. Ji  
Hunan Provincial Key Laboratory of Chemical Power Sources  
College of Chemistry and Chemical Engineering  
Central South University  
Changsha, 410083, China  
E-mail: hs-hou@csu.edu.cn

 Supporting information for this article is available on the WWW under  
<https://doi.org/10.1002/batt.201900030>

the charge/discharge platform, and hence decrease the energy density of the full cells, showing that the high capacity under 0.8 V of carbon material is a very important index. Given this, co-doping of the S and P with low doping amounts may be a good approach to enhance the capacity of the carbon materials during the voltage window of 0.01–1.0 V. As mentioned above, it is clear that heteroatoms modified hierarchical bubble-like carbon material with fast mass transfer pathway and expanded interlayer distance are very attractive anodes for the SIBs. However, it is a big challenge to introduce desired heteroatoms into carbon materials with hierarchical bubble-like structure. According to the survey, there are no related reports on the designation of hierarchical P,S co-modified bubble-like carbon. Based on this, an in-situ polymerization of the organic ketones appears out.

In this work, hierarchical P,S co-modified bubble-like carbon (PS-BC) material is successfully fabricated by in-situ catalytic polymerization reaction and carbonation process. Meaningfully, the morphology of the carbon material can be regulated by the type of doped heteroatoms. Furthermore, excellent charge/discharge performances are also achieved when utilized as anodes for SIBs due to its imitable structure. At last, the storage processes have been quantitatively evaluated, delivering a joint storage process of intercalation-controlled process and capacitive behavior. According to theoretical calculation, the excellent storage performance of the as-obtained samples can be assigned to the bonds between the doped-heteroatoms and carbon atoms, and abundant highly exposed edges of microcrystalline region. This work provides an alternative way for the development of heteroatoms modified hierarchical bubble-like materials.

## 2. Results and Discussions

### 2.1. Characterization of As-Obtained Samples

Figure 1a–d present the SEM and TEM images of the PS-BC, which are made up of plentiful interconnected and hierarchical

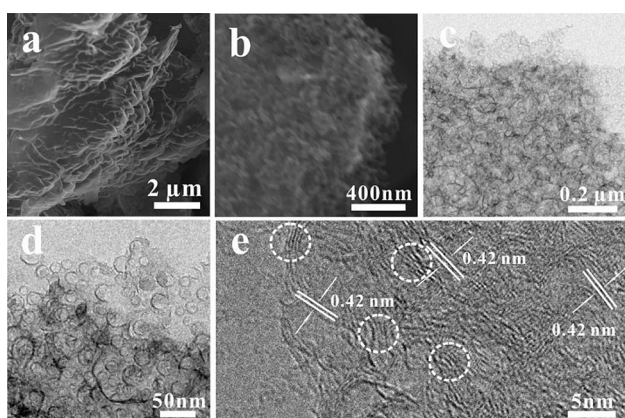


**Figure 1.** The SEM images (a–b), TEM images (c–d), and the HRTEM image (e) of PS-BC.

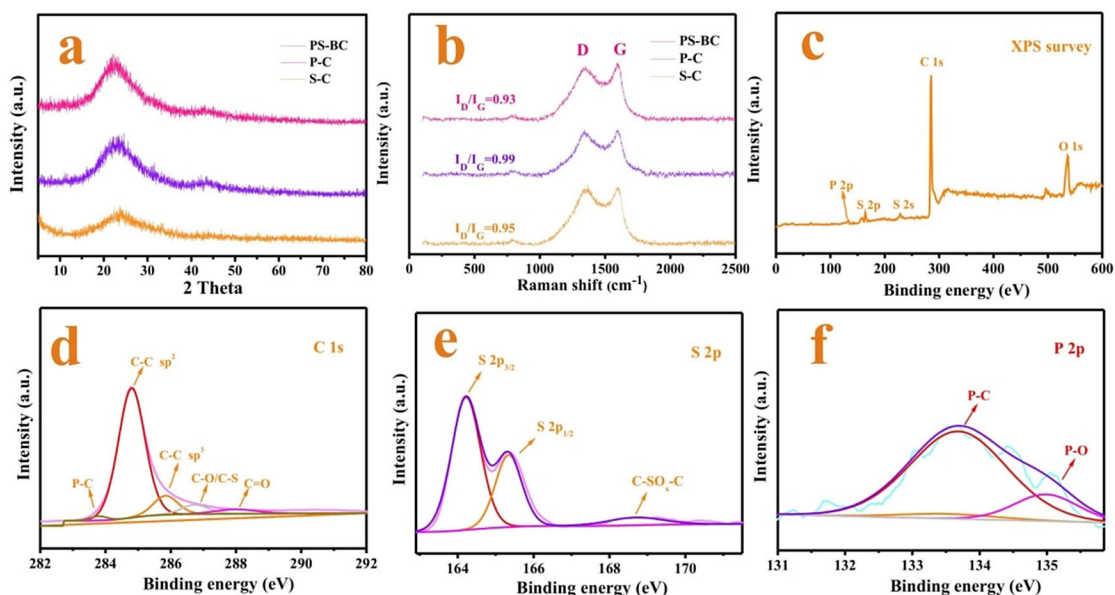
bubble-like porous carbons. This unique hierarchical bubble-like can provide numerous electron transfer path as well as shorten the mass transfer distance of the ions, thus efficiently improving the dynamic behavior of charging and discharging processes. Figure S1a shows the morphology structure of the intermediate product obtained from a carbonization treatment, in which lots of nanoparticles are evenly distributed, suggesting the formation process of the PS-BC. As the HRTEM image of PS-BC exhibited in Figure 1e, no large area of long range ordered structures are observed, inferring that the carbon are mainly composed of amorphous carbon. Besides, many micro-crystalline graphitized regions with short range ordered structure can be detected, exhibiting an interlayer distance of 0.42 nm. The interlayer distance is bigger than the minimum layer space for the intercalation of sodium ion (0.37 nm), which can boost the insertion/extraction rates of the sodium ion during the discharge/charge processes, and provide more active sites for the storage of  $\text{Li}^+/\text{Na}^+$ .<sup>[4a]</sup>

Figure 2a displays the XRD patterns of the S-C, P-C, and PS-BC, delivering a broad diffraction peak at 20 degree of about  $22^\circ$  and a small diffraction peak at 20 degree of about  $41^\circ$ , which are in good accord with the (002) and (100) planes of carbon materials. The dominated broad diffraction peaks at (002) diffraction of the related carbon materials infer the amorphous structure of the materials. Furthermore, according to the Bragg's equation and the 20 degree of (002) diffraction, an interlayer distance of 0.39, 0.40, and 0.42 nm for S-C, P-C, and PS-BC can be calculated, respectively, suggesting that the P,S elements with large covalent radius can effectively manipulate the interlayer distance of the carbon materials. Raman spectra (Figure 2b) list two characteristic peaks around at 1330 and  $1590\text{ cm}^{-1}$ , assigning to the D band and G band of carbonaceous materials, in which the value of ID/IG is an indicator to evaluate the degree of graphitization.<sup>[17]</sup> The ID/IG of PS-BC sample is 0.99, larger than that of the S-C (0.95) and P-C (0.93), which may be attributed to the increased structural distortion and defects brought by co-doping of S and P.<sup>[18]</sup>

To confirm the element contents and chemical environment of the S-C, P-C, and PS-BC, XPS tests have been conducted for the analysis. The definite C1s, O1s, S2p, and P2p peaks in Figure 2c infer the existence of C, O, S and P elements in the carbon skeleton, matching well with element compositions of 84.41, 12.57%, 2.01%, and 1.01%, separately (Table 1). As shown in Figure 2d, the C 1s peak can be deconvoluted into five bands. The large peak at 284.8 eV is ascribed to the graphitic structure ( $\text{C}=\text{Csp}^2$ ).<sup>[6a]</sup> The four small peaks located at 283.7, 285.9, 286.7, and 288.0 eV can be related to phosphorus-carbon single bonds (P-C), carbon-carbon single bonds of

**Table 1.** The XPS elemental content analysis and BET specific surface areas of the S-C, P-C, and PS-BC.

Samples	Element content [%]				BET [ $\text{m}^2\text{g}^{-1}$ ]
	C	S	P	O	
S-C	85.86	2.36	–	11.78	246.3
P-C	88.13	–	1.02	10.85	161.6
PS-BC	84.41	2.01	1.01	12.57	671.6



**Figure 2.** a) and b) are the XRD pattern and Raman spectra of PS-BC. c), d), e), and f) are the XPS survey of PS-BC, high-resolution XPS spectra of C1s, S2p, and P2p, respectively.

defects ( $\text{C}-\text{Csp}^3$ ), and carbon-oxygen/carbon-sulfur bonds ( $\text{C}-\text{O/C-S}$ ), carbon-oxygen double bonds ( $\text{C=O}$ ), respectively.<sup>[5b,15c,19]</sup> Figure 2e is the high resolution spectrum of S2p, and the three peaks positioned at 164.2, 165.2 and 168.7 eV can be attributed to  $\text{S}2\text{p}_{3/2}$ (C-S),  $\text{S}2\text{p}_{1/2}$ (C-S) and oxidized state sulfur species ( $\text{C-SO}_x\text{-C}$ ).<sup>[20]</sup> In addition, the XPS spectra for P2p can be deconvoluted into two featured peaks centered at 133.6 eV and 135.1 eV (Figure 2f), corresponding to P-C and P-O bond, respectively.<sup>[8,21]</sup> As mentioned above, it mightily proves that the P and S elements have been effectively incorporated into the skeleton structure of the carbon materials, which proficiently extend the interlayer distances of carbon materials.

As listed in Figure 3, the  $\text{N}_2$  adsorption-desorption isotherms of S-C, P-C, and PS-BC show a typical IV isotherm shape with a hysteresis loop, suggesting the co-presence of the microporous and mesoporous structure. The BET specific surface area of PS-BC is  $671.6 \text{ m}^2 \text{ g}^{-1}$  (Figure 3c and Table 1), much larger than that of S-C ( $246.3 \text{ m}^2 \text{ g}^{-1}$ , Figure 3a and Table 1), P-C ( $161.6 \text{ m}^2 \text{ g}^{-1}$ , Figure 3b and Table 1). Large specific surface area of PS-BC can assurance enough contact between the electrolyte and active materials due to the adequate space and plentiful networks for the diffusion of  $\text{Na}^+$ . Furthermore, the large surface area also can enhance the capacity of the carbon materials for sodium/lithium storage through a fast surface capacitive process. Furthermore, as shown in the Figure 3, the pore diameter distributions of the S-C and PS-BC are separately centered at 1.9 and 3.8 nm, while the pore diameter distribution of the P-C locates at 1.9 and 3.9 nm, presenting that the type of heteroatoms will have an impact on the pore structure and surface area of the carbon materials.

As exhibited in Figure 4, the SEM and TEM images of the S-C, P-C, and PS-BC are also provided to further recognize the influence of different heteroatoms on the morphologies. The S-C, P-C, and PS-BC deliver a nanosheet structure (Figure 4a),

a pleated nanosheet structure (Figure 4b), and hierarchical bubble-like structure (Figure 4c), respectively, indicating that the introduction of heteroatoms can effectively modify the surface structure of the carbon materials, which is consistent with some previous reports.<sup>[20b,22]</sup> The interlayer distances of the S-C, P-C, and PS-BC are 0.39, 0.40, and 0.42 nm, exhibiting the fact that the doping of the heteroatoms with large radius can efficiently expand the interlayer distances, which is in good accord with the XRD results above. In addition, the short-range crystalline domains can boost the transport rate of charge and stabilize the structure of the carbon materials during the fast insertion/extraction processes of  $\text{Li}^+/\text{Na}^+$ .<sup>[5a,23]</sup>

As mentioned above, a possible mechanism for the construction of PS-BC is offered in Scheme 1. Firstly, the aldol condensation reaction of acetone is happened under the catalysis of base, in which some reactions have also taken place with heteroatom sources and bases. Secondly, the as-obtained chain intermediates are stacked to form a carbon quantum dots (CQDs). Thirdly, the CQDs are further stacked into blocks due to hydrogen bonding with numerous sodium hydroxide particles evenly distributed among them. Subsequently, the polymer intermediates convert into carbon materials during the pyrolysis process, in which sodium hydroxide acts as activator and templating agent, which was hereafter transformed to sodium carbonate. Lastly, the PS-BC can be attained through a post acid treatment.

## 2.2. Quantum Chemistry Calculations

To further understand the existence state of heteroatoms and role in modifying the electrochemical activity in carbon materials, quantum chemistry calculations based on density functional theory (DFT) were carried out. The related calculated

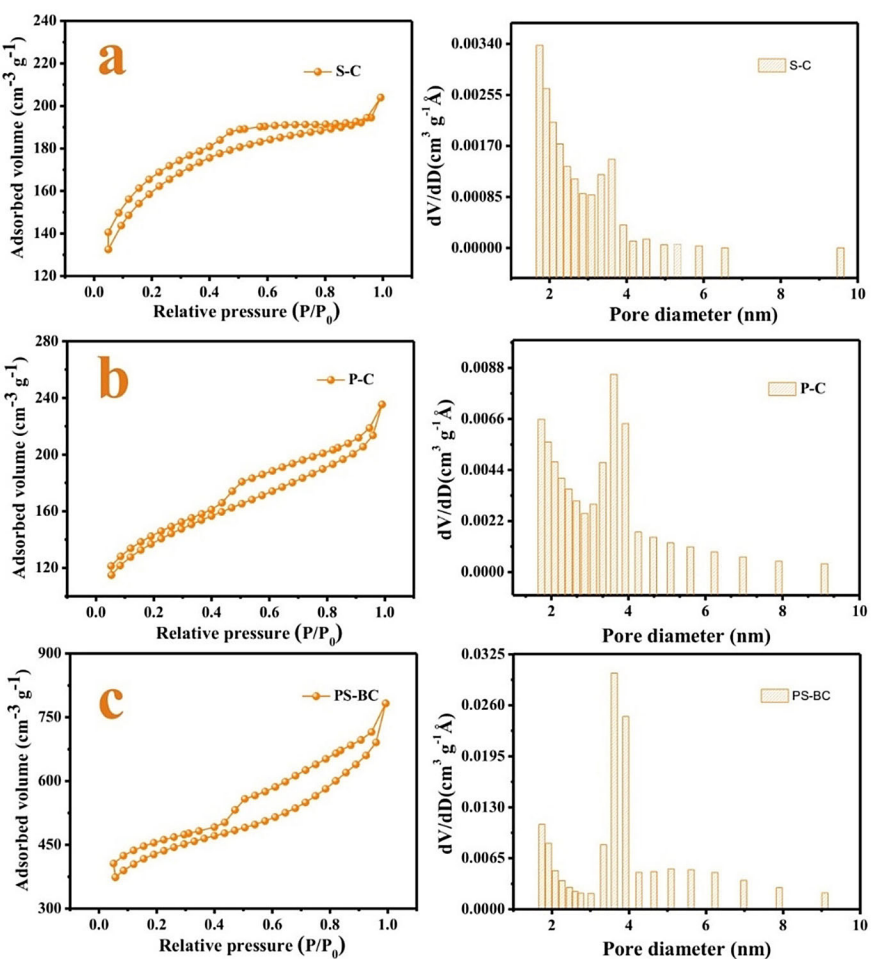
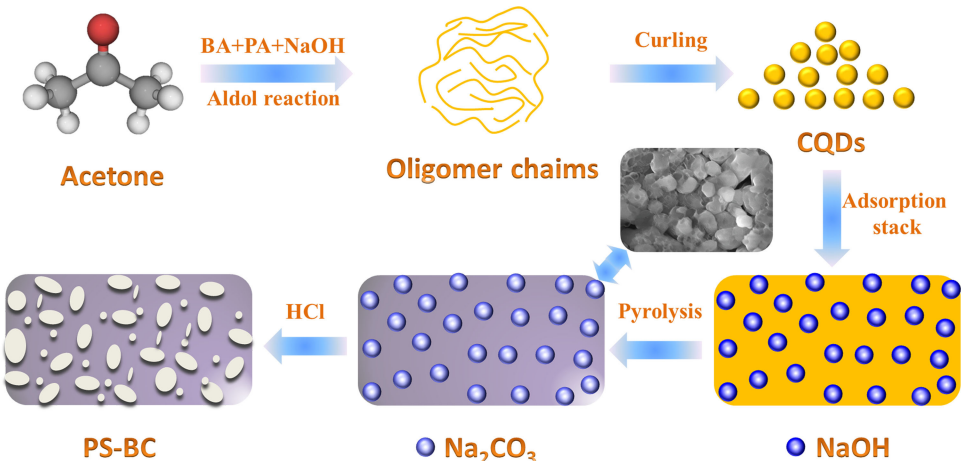


Figure 3. The N<sub>2</sub> adsorption/desorption isotherms and pore distributions of the S-C (a), P-C (b), and PS-BC (c).



Scheme 1. The design preparation of hierarchical P,S co-modified bubble-like carbon (PS-BC).

results of frontier molecular orbitals and sum of the energy are based on the last optimized structure of the carbon materials (Figure 5 and S2). Frontier molecular orbitals, containing the highest occupied molecular orbitals (HOMO) and lowest unoccupied molecular orbitals (LUMO) are persuasive results for

the understanding of chemical reactivity, in which electrons donation capacity of a molecule is directly connected to the HOMO, while the electrons donation capacity and spatial distribution of valence electron are mainly dependent on the LUMO. Hence, the energy gap ( $\Delta E_{\text{gap}}$ ) between HOMO and

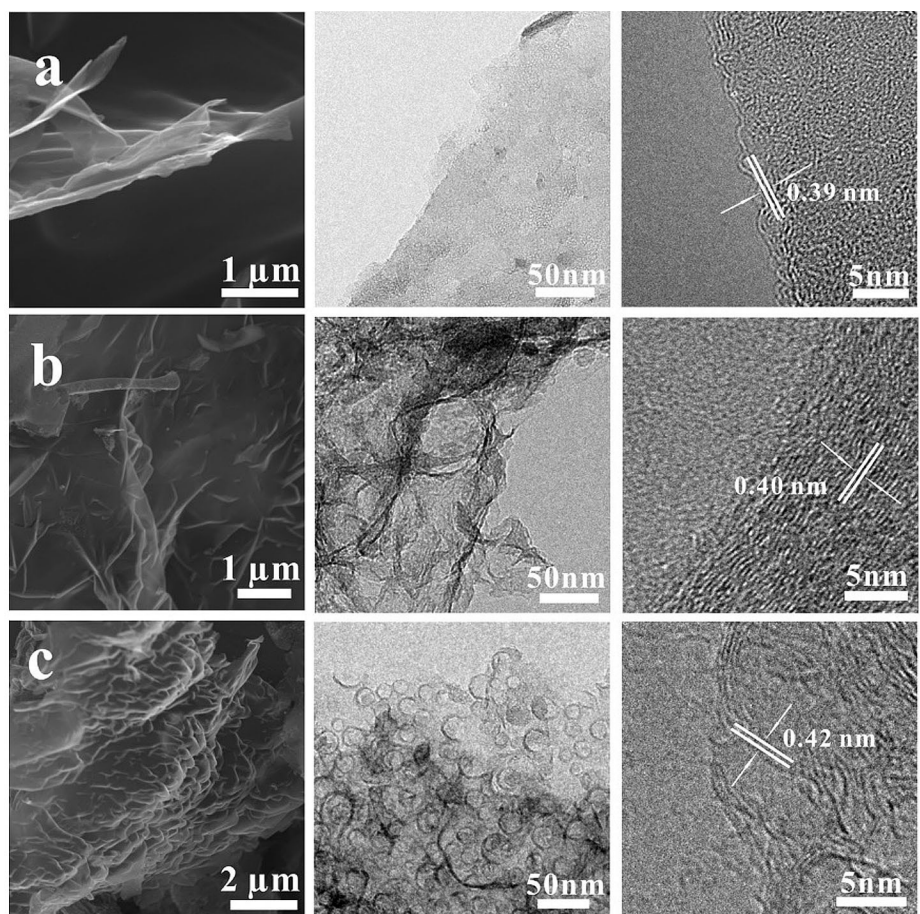


**Figure 4.** The SEM images, TEM images, and HRTEM images of S–C (a), P–C (b), and PS–BC (c).

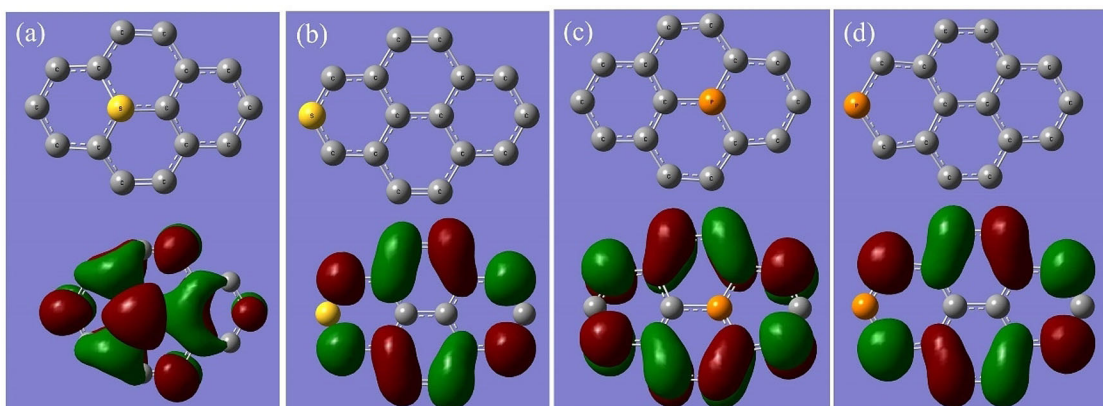


**Figure 5.** The simplified model and its frontier molecular orbitals (HOMO and LUMO) of the SC-1 (S-doped in perfect graphite structure, a), the SC-2 (S-doped on the edges of graphite structure, b), the PC-1 (P-doped in perfect graphite structure, c), the PC-2 (P-doped on the edges of graphite structure, d)

LUMO can be applied to measure the stability of a specified molecule. The larger the gap, the more stable of the related material. Figure 5 exhibits the HOMO and LUMO of related materials, and the detailed data are listed in Table 2. Obviously, HOMO and LUMO of the materials are mostly confined on the graphite sheet, signifying that the excellent conductivity of the materials.<sup>[24]</sup> Different from the HOMO and LUMO of C (Figure S2), the HOMO and LUMO of the SC-1 are mainly

localized at the center of the small model, showing that the active sites are derived from the central part.<sup>[25]</sup> While for the SC-2, the active sites mainly come from the edges, indicating that the doping of the heteroatoms can effectively modify the active sites of the carbon materials. As presented in Table 2, the HOMO-LUMO gaps of the C, SC-1, SC-2, PC-1 and PC-2 calculated from B3LYP are 3.85, 0.88, 1.24, 1.07, and 1.30 eV, demonstrating that the heteroatoms-doping can effectively

**Table 2.** The energy gaps of HOMO and LUMO of the different materials. Unit is eV.

Simplified models	B3LYP/6-31G(d) HOMO	LUMO	$\Delta E_{\text{gap}}$
C	-5.33	-1.48	3.85
SC-1	-6.80	-5.92	0.88
SC-2	-6.00	-4.76	1.24
PC-1	-6.50	-5.43	1.07
PC-2	-2.94	-1.64	1.30

enhance the reactive activity and electronic conductivity. More importantly, the energy gaps of the SC-1 and PC-1 are smaller than that of the SC-2 and PC-2, respectively, which indicates that the edge-doping structure is more stable. Furthermore, the  $\Delta G_s$  and  $\Delta G_p$  corresponding to the conversion from the SC-1 to SC-2 and PC-1 to PC-2 are -1371.56 and -73.51 kJ/mol, respectively, indicating that the edge-doping is more likely to occur,<sup>[26]</sup> which illustrates the doped sites of the heteroatoms in the carbon materials as well as the heteroatoms-doping will

produce more highly exposed edges through the construction of short-order structure or defects in the graphite layers.

### 2.3. Electrochemical Storage Properties for Sodium

Figure 6a and 6b list the sodium storage performances of S-C, P-C, and PS-BC in the potential window of 0.01–3 V at a current density of 0.1 A g<sup>-1</sup>. The first discharge/charge capacities of S-C, P-C, and PS-BC are 978.5/442.7, 1271.5/545.8, and 1240.8/628.6 mAh g<sup>-1</sup>, demonstrating first coulombic efficiencies of 45.2%, 42.9%, and 50.7%, respectively (Figure S3). The relatively low first coulombic efficiencies of the as-obtained samples can be allocated to the some irreversible reactive processes of the organic electrolyte, surface functional groups, and active materials, or the construction of SEI film, which is comparable to that of the other literatures.<sup>[4d,5a,20c,27]</sup> Excitingly, the first coulombic efficiency of the PS-BC is higher than that of S-C and P-C, which can be ascribed to the modification of heteroatoms. Besides, the coulombic efficiencies of the S-C,

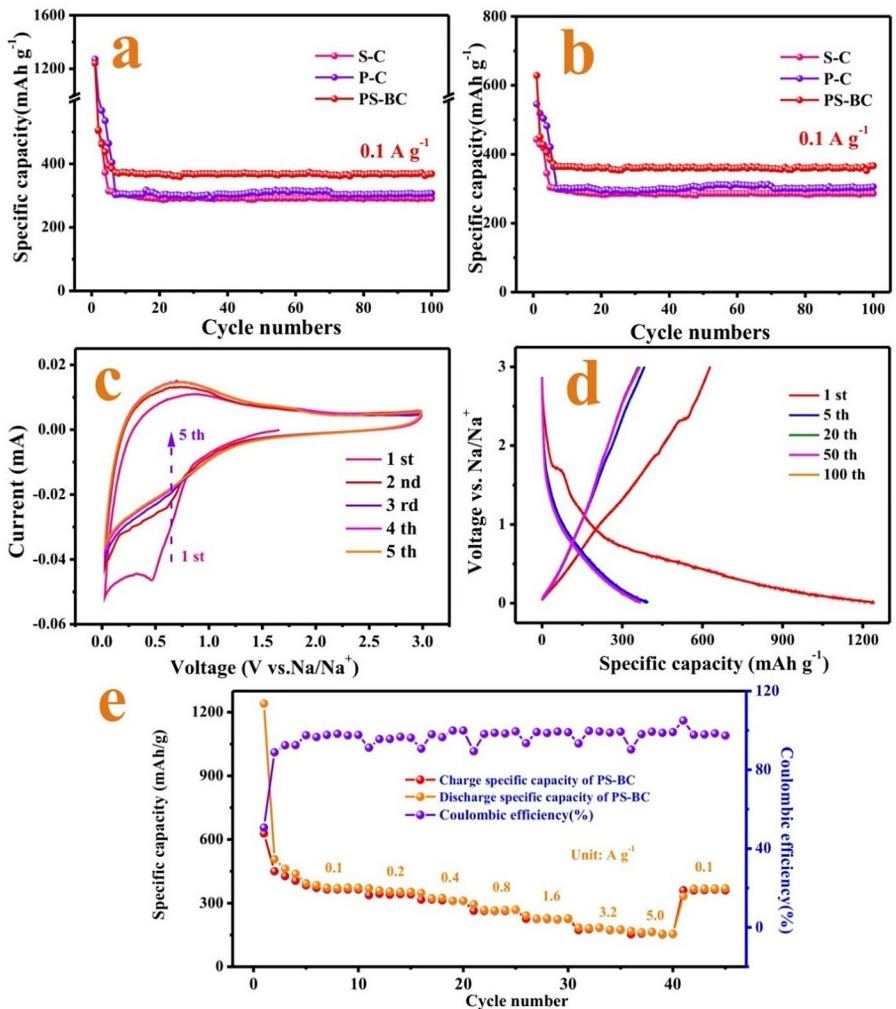


**Figure 6.** a) and b) are the cycle performances of the as-prepared samples at 0.1 A g<sup>-1</sup> within the potential range from 0.01 to 3 V (vs Na<sup>+</sup>/Na), separately. c) and d) are the CV curves under a scan rate of 0.1 mVs<sup>-1</sup> and galvanostatic discharge/charge profiles at a current density of 0.1 A g<sup>-1</sup> of the SIBs using the PS-BC as anode. e) The rate capability of half-cells utilizing PS-BC as anode.

P-C, and PS-BC are close to 100% after some cycles. The S-C, P-C, and PS-BC exhibit reversible discharge capacities of 291.2, 307.3, and 368.4 mAh g<sup>-1</sup> at a current density of 100 mA g<sup>-1</sup> after 100 cycles. The higher specific capacity of the PS-BC relative to S-C and P-C can be attributed to the expanded interlayer distances and enhanced surface capacitive behavior derived from the doping of heteroatoms.

The electrochemical storage properties of the PS-BC electrodes for SIBs are characterized by cyclic voltammetry (CV) methods through employing Na-half cell between 0.01 V and 3 V at a sweep rate of 0.1 mV s<sup>-1</sup>. As shown in Figure 6c, a large and broad irreversible cathodic peak located at about 0.5 V is detected in the initial cycle and vanishes in the following cycles, assigning to the uncertain irreversible reactions of sodium species, surface functional groups, and electrolyte, and the establishment of solid-electrolyte interphase (SEI).<sup>[4f,5a,20c]</sup> From the second cycle, a long and broad cathodic slope range from 1.1 to 0.01 V can be discovered, relating to the insertion of sodium ions into the extended graphitic interlayers, or the sodium ions storage in the surface functional groups and defects, which occur within a broad voltage window, and separately match with the diffusion-controlled behavior and capacitive-dominated behavior.<sup>[4b,d,28]</sup>

Figure 6d displays the galvanostatic charge/discharge profiles of PS-BC with different cycles at 0.1 A g<sup>-1</sup> in the potential range of 0.01–3 V (vs. Na<sup>+</sup>/Na), exhibiting three small plateaus in the initial discharge process. Besides, the PS-BC delivers discharge/charge capacities of 1240.8/628.6, 395.6/383.1, 368.1/359.9, 368.1/359.7, 368.4/366.4 mAh g<sup>-1</sup> at 1st, 5th, 20th, 50th and 100th, respectively, presenting a good cycling performance. During the discharge profiles, the long slope located at a broad potential region (0.01–1 V) maybe be allocated to the reversible insertion/extraction of Na<sup>+</sup> into/out of the carbon layers or reversible sodium storage on the surface active sites,<sup>[4d,6a,28]</sup> which are the main sources of the storage capacity, matching with the cyclic voltammetry (CV) results (Figure 6c).

High rate capacity is a key parameter to assess the electrochemical performance of the electrode materials. The rate performance of PS-BC is excellent (Figure 6e), and reversible capacities of 364.7, 340.6, 310.7, 268.5, 226.2, 172.9, 159.8 mAh g<sup>-1</sup> are gained at 0.1, 0.2, 0.4, 0.8, 1.6, 3.2, 5 A g<sup>-1</sup>, respectively. When the current density returns to 0.1 A g<sup>-1</sup>, the reversible capacity increases again to 360.2 mAh g<sup>-1</sup>, signifying an extraordinary mechanical stability in the fast charge/discharge procedures. Besides, the contrast of sodium storage performance for PS-BC and other carbon anodes described in earlier works is presented in Table S1. The superior high-rate performance of the PS-BC can be ascribed to the co-modification of P and S elements, expanding the interlayer spacing and constructing a hierarchical bubble-like structure with high surface area, which can offer fast transfer paths for electrons/sodium ions, dismiss volume expansion, and enhance the stability of the carbon materials. Furthermore, the surface functional groups, such as the C-S, C-P, and highly exposed edges may also provide a fast-capacitive capacity.

## 2.4. Detailed Kinetic Exploration of PS-BC for Sodium Storage

According to the previous reports, the storage mechanisms of the carbon materials can be assigned into two parts: (1) diffusion dominated mechanism derived from the intercalation behavior of the Na<sup>+</sup> into the graphite crystallite region with large interlayer distances (>0.37 nm), (2) surface capacitance-controlled mechanism, containing the double-layer capacitance process and pseudo-capacitance behavior.<sup>[28–29]</sup> In order to confirm the fact that capacity comes from which storage mechanism, the cyclic voltammograms(CVs) measurements under different sweep rates range from 0.1 to 0.9 mV s<sup>-1</sup> are collected and presented in Figure 7a–7c. For a diffusion dominated mechanism, the current (*i*) keeps linear connection with the square root of the sweep rate (*v*) [Equation (1)].<sup>[29]</sup> As for the surface capacitance-controlled mechanism, *i* shows a linear association with *v* [Equation (2)].<sup>[29]</sup> Thence, the two mechanisms can be expressed in an [Equation (3)], in which *a* and *b* are modifiable value.<sup>[28]</sup> The value of *b* approach to 0.5 suggests that the diffusion dominated mechanism provides most of the capacity, while the value of *b* close to 1 indicates that surface capacitance-controlled mechanism affords most of the capacity. In this work, the *b*-value of S-C, P-C, and PS-BC are 0.73, 0.56, and 0.88, respectively (Figure 7d), showing that the capacity of P-C generally comes from the diffusion dominated process, while the capacity of S-C and PS-BC originate from collaborative processes of the diffusion dominated behavior and surface capacitance-controlled behavior.

$$i = nFAC^* D^{1/2} v^{1/2} (\alpha nF/RT)^{1/2} \pi^{1/2} \chi(bt) \quad (1)$$

$$i = vC_d A \quad (2)$$

$$i = av^b \quad (3)$$

$$i(v) = k_1 v + k_2 v^{1/2} \quad (4)$$

Furthermore, the whole capacitance contributions can be quantitatively distinguished at a certain scan rate by Equation (4), where  $k_1 v$  and  $k_2 v^{1/2}$  separately stand for the capacity stemmed from surface capacitive process and insertion process.<sup>[28]</sup> As shown in Figure 7e, the  $k_1$  and  $k_2$  can be easily achieved via plotting  $i(v)/v^{1/2}$ , in which  $k_1$  and  $k_2$  are the slope and intercept of the straight line, respectively. As listed in Figure 7f–7h, the capacitive charge ratios in the total charge of S-C, P-C, and PS-BC are 69.8%, 33%, and 82.6% at the same scan rate of 0.5 mV s<sup>-1</sup>, respectively. At the same time, the capacitive charge ratios in the total charge of PS-BC under various scan rates are also calculated and listed in Figure 7i, delivering an increasing trend range from 58.8% to 90.5% with the scan rate increasing from 0.1 to 0.9 mV s<sup>-1</sup>, which demonstrate that the capacity of the PS-BC mainly originates from the surface-prompted capacitive processes under fast discharge/charge processes and illuminate the remarkable rate capability of PS-BC from a principle perspective.

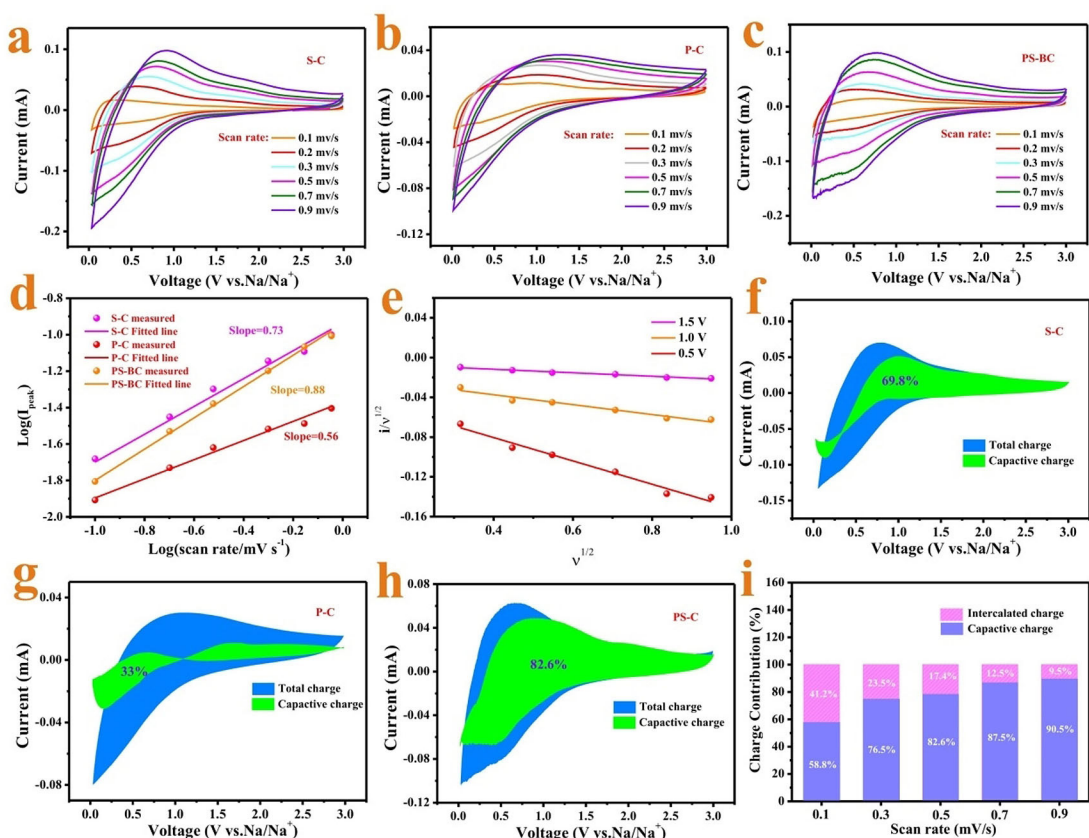


**Figure 7.** a), b), and c) are the CV curves collected at various scan sweep rates range from 0.1 to 0.9 mVs<sup>-1</sup> of S-C, P-C, and PS-BC within the potential range from 0.01 to 3 V (vs Na<sup>+</sup>/Na), separately. d) The fitting straight line plotted by the log (sweep rate/mVs<sup>-1</sup>)-log (I<sub>peak</sub>) of the as-obtained samples. e) The fitting straight line plotted by the log (sweep rate/mVs<sup>-1</sup>)-log (I<sub>peak</sub>) of PS-BC under different potential windows. f), g), and h) are the capacitive contributions ratios of S-C, P-C, and PS-BC specimens under the same sweep rate of 0.5 mVs<sup>-1</sup>, respectively. i) Capacitive contributions of PS-BC at different scan rates between 0.1 and 0.9 mVs<sup>-1</sup> under a positive potential of 0.5 V.

## 2.5. Storage Properties and Kinetic Survey of PS-BC for Lithium

The storage properties of PS-BC for lithium are also assessed in details by utilizing the standard half-cell system. Figure 8a displays cyclic voltammetry (CV) curves of PS-BC anodes measured at a scan rate of 0.1 mVs<sup>-1</sup>, coinciding with those of formerly reported carbon-based electrodes.<sup>[30]</sup> In the initial cycle, a noticeable reduction slope range from 1.2 to 0.25 V can be related to uncertain irreversible reaction between the electrolyte and active materials, the establishment of a solid electrolyte interphase (SEI) on the surface of the electrode, which vanishes in the next cycles.<sup>[18c,31]</sup> Note that the CV curves almost overlapped in the subsequent cycles, inferring the formation of a stable SEI layer. Besides, the peak located at 0.1 V is attributed to insertion of the Li ions into the graphitic layers, while the long slope above 0.1 V may be ascribed to the surface capacitive behaviour.<sup>[18c]</sup> The two distinguishing redox couples situated at 1.6/2.3 V and 0.75/1.8 V could be assigned to the multistep reduction mechanism between S and Li, comparable to that reported in the Li-S batteries.<sup>[32]</sup> Figure 8b displays the capacity of the PS-BC anode at diverse current densities range from 0.1 to 5 A g<sup>-1</sup>. A reversible capacity of 903.6, 794.2, 678.9, 555.2, 433.6, and 341.6 mAh g<sup>-1</sup> can be

achieved at a current density of 0.1, 0.2, 0.4, 0.8, 1.6, and 3.2 A g<sup>-1</sup>, respectively. Even at a great current density of 5 A g<sup>-1</sup>, a high capacity of 286.2 mAh g<sup>-1</sup> still can be attained. What's more, after 100 cycles at different current densities, the PS-BC anode reinstates a reversible capacity of 893.8 mAh g<sup>-1</sup> when the current density reduces again to 0.1 A g<sup>-1</sup>, validating an exceptional high rate property. To assess the kinetic storage behavior of PS-BC for lithium, the cyclic voltammograms (CVs) curves under different scan rates are presented listed in Figure 8c. The b-value is 0.92 (Figure 8d), showing that the capacity of PS-BC mainly comes from the surface capacitance-controlled behavior. Moreover, as depicted in Figure 8e, the capacitive contribution of PS-BC for lithium storage is 78.8% at a scan rate of 0.5 mVs<sup>-1</sup>, which is similar to the results for sodium storage.

Therefore, we have confirmed the extraordinary electrochemical storage properties of PS-BC for the anodes of SIBs and LIBs. The subsequent aspects may be utilized to explicate the high capacity, good cycling stability and outstanding rate capability of the hierarchical P,S co-modified bubble-like carbon (Figure 9). First, the expanded interlayer spacing and enhanced electronic conductivity derived from the large radius doping of P and S can provide more active site for the Na<sup>+</sup>/Li<sup>+</sup> storage. Second, the highly exposed edges originated from the short-

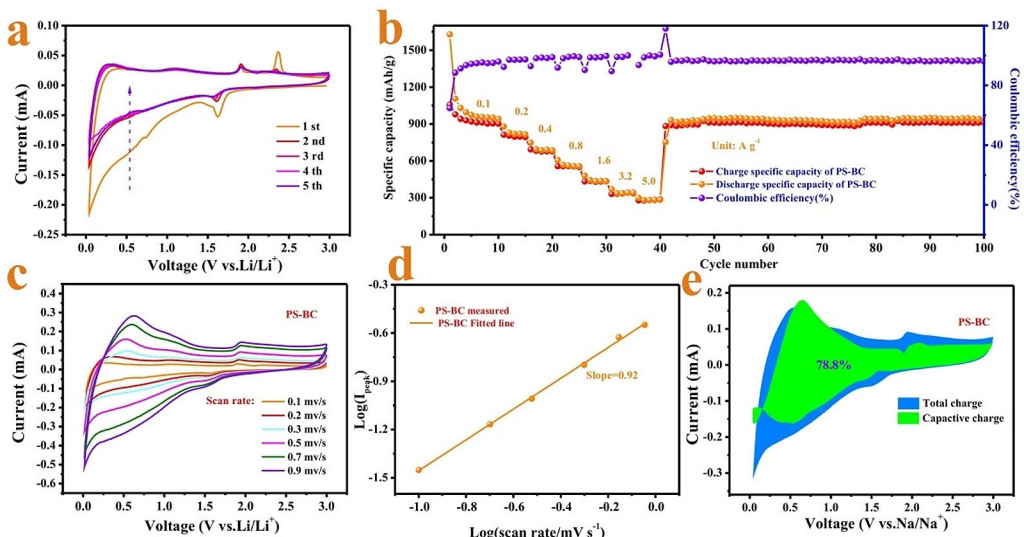


**Figure 8.** a) The CV curves of PS-BC remarked at  $0.1 \text{ mV s}^{-1}$  within a voltage range from 0.01 to 3 V (vs  $\text{Li}^+/\text{Li}$ ). b) The rate performances and cycle properties of the LIBs utilizing PS-BC as anode under different current densities. c) The CV curves collected at diverse scan rates range from 0.1 to  $0.9 \text{ mV s}^{-1}$  of PS-BC. d) The fitting line plotted by the log (sweep rate/ $\text{mV s}^{-1}$ )-log ( $I_{\text{peak}}$ ) of the as-obtained sample for LIBs. e) The capacitive contributions ratios of PS-BC anode for LIBs at a scan rate of  $0.5 \text{ mV s}^{-1}$ .

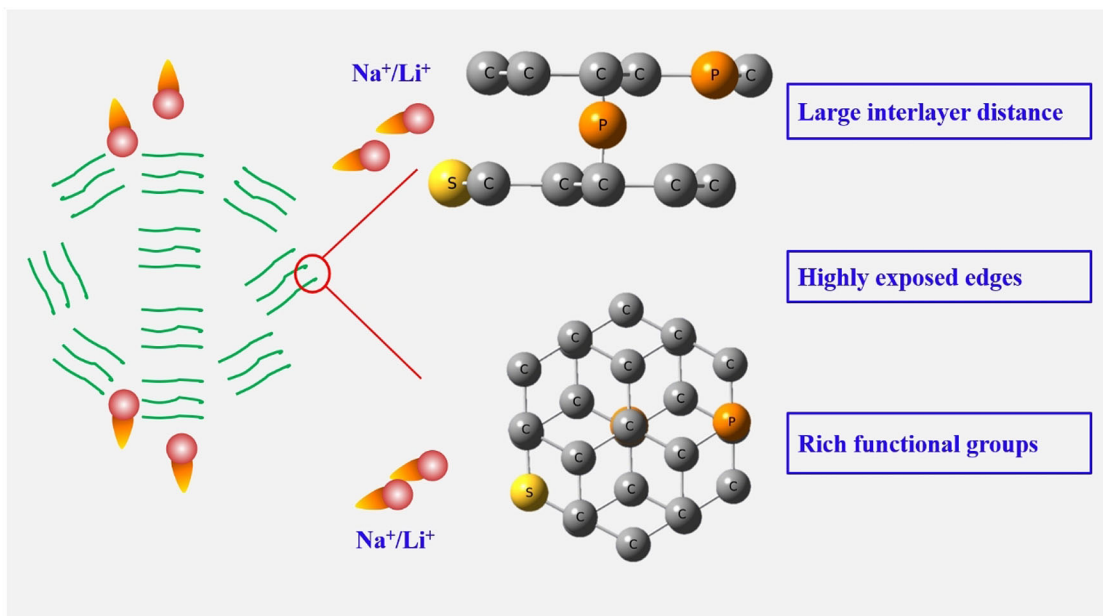


**Figure 9.** The simplified model of P,S-codoped carbon materials for  $\text{Na}^+/\text{Li}^+$  storage

range ordered structure or defects in carbon materials would shorten the diffusion distance of  $\text{Na}^+/\text{Li}^+$  in graphite layers. Third, the rich surface functional groups, such as the C–S and C–P may also provide a fast-capacitive capacity. At last, the hierarchical bubble-like structure with countless opened gaps, high surface area, as well as micropores and mesopores, can proficiently guarantee the uninterrupted supplement of electrolyte, offer fast ion transport channels for  $\text{Na}^+/\text{Li}^+$ , and reduce  $\text{Na}^+/\text{Li}^+$  diffusion distance, delivering a huge capacitance contribution and a high rate capability.

### 3. Conclusions

A general strategy for the preparation of heteroatoms-doped carbon materials has been provided and a hierarchical P,S co-modified bubble-like carbon with enlarged interlayer spacing is initially prepared. Interestingly, the morphology of the carbon materials can be effectively tuned by the type of doping heteroatoms. Impressively, theoretical calculation results demonstrate that the P,S doping can enhance the electronic conductivity, produce rich exposed edges, enlarge interlayer distance, and generate large amount of surface functional

groups, well explaining the remarkable storage performance for sodium and lithium of as-obtained carbon materials from microscopic perspective. Additionally, the kinetic surveys suggest that the capacity is mainly derived from fast surface-dominated capacitive process in rapid discharge/charge processes for the optimum sample, showing that the excellent rate capability of a material can be achieved by a unique surface structure as well as abundant surface-active sites. Meaningfully, this work provides a general approach to the large batch preparation of desirable heteroatoms-doped carbon materials with unique structure, demonstrating potential industrial application value.

## Experimental Section

### Materials Synthesis

Typically, 0.25 mol NaOH (Alfa Aesar, AR), 0.006 mol benzenesulfonic acid(BA) (Alfa Aesar, AR), 0.006 phenylphosphonic acid (PA) (Alfa Aesar, AR), and 0.50 mol acetone (Shanghai Titan Scientific Co.,Ltd. AR) were put into a 100 mL beaker. After stirring for 60 minutes, a tan mixture was acquired and then sealed it by sealing bag. Resting reaction for 5 days, a black product was acquired and then calcined for 2 hours under 850 °C with inert gas protection. The heating ramp is 5 °C min<sup>-1</sup>. After cooling down, adding suitable amount of dilute hydrochloric acid (1 M), and washing with deionized water to neutral, the hierarchical P,S co-modified bubble-like carbon (PS-BC) was obtained. As a contrast, the carbon materials prepared only from 0.006 mol benzenesulfonic acid and 0.006 mol phenylphosphonic acid were separately flagged as S-C and P-C.

### Materials Characterization

The structural and topographical characterization of the as-prepared carbon materials were collected by an X-ray diffractometer (XRD, Rigaku) ( $V=30$  kV,  $I=25$  mA, 0.15418 nm), Raman spectroscopy (DXR, Thermo-Fisher Scientific), ASAP 2010 instrument (adsorption/desorption isotherms), VG Multi Lab 2000 system (X-ray photoelectron spectroscopy), Hitachi S-4800 microscope (Scanning electron microscopy), and JEOL-2010 instrument (transmission electron microscopy), respectively.

### Electrochemical Measurements

Take 15 mg of binder CMC (carboxymethyl cellulose) (Alfa Aesar) dissolved in moderate water. After stirring for 6 h, a mixture made up of 70 mg active materials (S-C, P-C, and PS-BC) and 15 mg Super P (conductive carbon, TIMCAL) was added in it. Keeping stir for 12 hours, a slurry was obtained and then uniformly distributed on the Cu foils and dried at 100 °C for 12 h under vacuum condition. The mass loading of the electrode material is about 0.9–1.1 mg cm<sup>-2</sup>. Subsequently, the sodium metal (Sinopharm Chemical Reagent Co., Ltd, 99.9%), 1 mol L<sup>-1</sup> NaClO<sub>4</sub> solution in propylene carbonate (Alfa Aesar, AR), the as-fabricated electrode sheet, and polypropylene film (Celgard 2400) were utilized as the counter, electrolyte, the working electrodes, and separator to assemble the CR2016-type half-cells, respectively. The galvanostatic electrochemical charge/discharge processes under different current densities with a potential window range from 0.01 to 3 V and cyclic voltammetry (CV) curves with changed sweep rates were separately

observed through an Arbin BT2000 instrument and a Multi Autolab M204 electrochemical station.

### First-Principles Calculations

All the first-principles calculations were collected by utilizing the Gaussian 09 (D01 version). In order to counterpoise the calculation precision and computational cost, the simplified calculation models (heteroatoms-doped single layer graphite) are constructed to signify the as-related carbon materials. The C, SC-1, SC-2, PC-1, PC-2 are corresponding to the graphite, the S-doped carbon (S-doped in perfect graphite structure), the S-doped carbon (S-doped on the edges of graphite structure), the P-doped carbon (P-doped in perfect graphite structure), the P-doped carbon (P-doped on the edges of graphite structure). To obtain the electronic and energy information of the carbon materials, the B3LYP/6-31G(d) basis set is employed in these calculations.<sup>[33]</sup>

### Acknowledgements

This work was financially supported by National Key Research and Development Program of China (2018YFC1901605), the National Postdoctoral Program for Innovative Talents (BX201600192), Hunan Provincial Science and Technology Plan (2017TP1001).

### Conflict of Interest

The authors declare no conflict of interest.

**Keywords:** electrochemistry · heteroatom-doping · hierarchical carbon · materials science · sodium-ion batteries

- [1] K. Gong, F. Du, Z. Xia, M. Durstock, L. Dai, *Science* **2009**, *323*, 760.
- [2] a) M. Zheng, A. Jagota, E. D. Semke, B. A. Diner, R. S. McLean, S. R. Lustig, R. E. Richardson, N. G. Tassi, *Nat. Mater.* **2003**, *2*, 338; b) C. Moreno-Castilla, *Carbon* **2004**, *42*, 83–94.
- [3] Y. Shao, J. Wang, H. Wu, J. Liu, Ilhan, A. Aksay, Y. Lin, *Electroanalysis* **2010**, *22*, 1027–1036.
- [4] a) Y. Cao, L. Xiao, M. L. Sushko, W. Wang, B. Schwenzer, J. Xiao, Z. Nie, L. V. Saraf, Z. Yang, J. Liu, *Nano Lett.* **2012**, *12*, 3783–3787; b) C. Chen, Y. Wen, X. Hu, X. Ji, M. Yan, L. Mai, P. Hu, B. Shan, Y. Huang, *Nat. Commun.* **2015**, *6*, 6929; c) C. Bommier, T. W. Surta, M. Dolgos, X. Ji, *Nano Lett.* **2015**, *15*, 5888–5892; d) X. Xu, C. Chen, J. Xie, B. Zhang, L. Miao, J. Cai, Y. Huang, L. Zhang, *Adv. Energy Mater.* **2016**, *6*, 1501929; e) L. Fu, K. Tang, K. Song, P. A. van Aken, L. Yu, J. Maier, *Nanoscale* **2014**, *6*, 1384–1389; f) W. Li, M. Zhou, H. Li, K. Wang, S. Cheng, K. Jiang, *Energy Environ. Sci.* **2015**, *8*, 2916–2921.
- [5] a) J. Xu, M. Wang, N. P. Wickramaratne, M. Jaroniec, S. Dou, L. Dai, *Adv. Mater.* **2015**, *27*, 2042–2048; b) J. Liang, Y. Jiao, M. Jaroniec, S. Z. Qiao, *Angew. Chem. Int. Ed. Engl.* **2012**, *51*, 11496–11500; c) D. Datta, J. Li, V. B. Shenoy, *ACS Appl. Mater. Interfaces* **2014**, *6*, 1788–1795.
- [6] a) G. Zou, C. Wang, H. Hou, C. Wang, X. Qiu, X. Ji, *Small* **2017**, *1700762*; b) R. Song, H. Song, J. Zhou, X. Chen, B. Wu, H. Y. Yang, *J. Mater. Chem.* **2012**, *22*, 12369–12374.
- [7] a) K. Tang, L. Fu, R. J. White, L. Yu, M. M. Titirici, M. Antonietti, J. Maier, *Adv. Energy Mater.* **2012**, *2*, 873–877; b) Y. Li, Z. Wang, L. Li, S. Peng, L. Zhang, M. Srinivasan, S. Ramakrishna, *Carbon* **2016**, *99*, 556–563.
- [8] W. Yang, W. Yang, L. Kong, A. Song, X. Qin, G. Shao, *Carbon* **2018**, *127*, 557–567.
- [9] Q. Wei, H. Fan, F. Qin, Q. Ma, W. Shen, *Carbon* **2018**, *133*, 6–13.
- [10] S. Jiang, M. Chen, X. Wang, Y. Zhang, C. Huang, Y. Zhang, Y. Wang, *Chem. Eng. J.* **2019**, *355*, 478–486.

- [11] a) J.-Y. Hwang, S.-T. Myung, Y.-K. Sun, *Chem. Soc. Rev.* **2017**, *46*, 3529–3614; b) G. Zou, H. Hou, P. Ge, Z. Huang, G. Zhao, D. Yin, X. Ji, *Small* **2018**, *14*, 1702648.
- [12] a) H. Pan, Y. S. Hu, L. Chen, *Energy Environ. Sci.* **2013**, *6*, 2338–2360; b) Y. Jiang, G. Zou, W. Hong, Y. Zhang, Y. Zhang, H. Shuai, W. Xu, H. Hou, X. Ji, *Nanoscale* **2018**, *10*, 18786–18794.
- [13] P. Adelhelm, P. Hartmann, C. L. Bender, M. Busche, C. Eufinger, J. Janek, *Beilstein J. Nanotechnol.* **2015**, *6*, 1016–1055.
- [14] a) H. Hou, C. E. Banks, M. Jing, Y. Zhang, X. Ji, *Adv. Mater.* **2015**, *27*, 7861–7866; b) Y. Zhang, L. Yang, Y. Tian, L. Li, J. Li, T. Qiu, G. Zou, H. Hou, X. Ji, *Mater. Chem. Phys.* **2019**, *229*, 303–309; c) P. Ge, H. Hou, X. Cao, S. Li, G. Zhao, T. Guo, C. Wang, X. Ji, *Adv. Sci.* **2018**, *5*, 1800080.
- [15] a) Z. Wang, L. Qie, L. Yuan, W. Zhang, X. Hu, Y. Huang, *Carbon* **2013**, *55*, 328–334; b) G. Zou, H. Hou, C. W. Foster, C. E. Banks, T. Guo, Y. Jiang, Y. Zhang, X. Ji, *Adv. Sci.* **2018**, *1800241*; c) H. Hou, L. Shao, Y. Zhang, G. Zou, J. Chen, X. Ji, *Adv. Sci.* **2017**, *4*, 1600243.
- [16] L. Qie, W. Chen, X. Xiong, C. Hu, F. Zou, P. Hu, Y. Huang, *Adv. Sci.* **2015**, *2*, 1500195.
- [17] J. Ding, H. Wang, Z. Li, A. Kohandehghan, K. Cui, Z. Xu, B. Zahiri, X. Tan, E. M. Lotfabad, B. C. Olsen, D. Mitlin, *ACS Nano* **2013**, *7*, 11004–11015.
- [18] a) X. Sun, C. Wang, Y. Gong, L. Gu, Q. Chen, Y. Yu, *Small* **2018**, *14*, 1802218; b) Y. Qiao, M. Ma, Y. Liu, S. Li, Z. Lu, H. Yue, H. Dong, Z. Cao, Y. Yin, S. Yang, *J. Mater. Chem. A* **2016**, *4*, 15565–15574; c) W. Ai, Z. Luo, J. Jiang, J. Zhu, Z. Du, Z. Fan, L. Xie, H. Zhang, W. Huang, T. Yu, *Adv. Mater.* **2014**, *26*, 6186–6192; d) T. Akhter, M. M. Islam, S. N. Faisal, E. Haque, A. I. Minett, H. K. Liu, K. Konstantinov, S. X. Dou, *ACS Appl. Mater. Interfaces* **2016**, *8*, 2078–2087.
- [19] a) M. Latorre-Sánchez, A. Primo, H. García, *Angew. Chem.* **2013**, *52*, 11813; b) S. Yang, L. Peng, P. Huang, X. Wang, Y. Sun, C. Cao, W. Song, *Angew. Chem.* **2016**, *55*, 4016; c) C. E. B. Marino, P. A. P. Nascente, S. R. Biaggio, R. C. Rocha-Filho, N. Bocchi, *Thin Solid Films* **2004**, *468*, 109–112.
- [20] a) Z. Liu, H. Nie, Z. Yang, J. Zhang, Z. Jin, Y. Lu, Z. Xiao, S. Huang, *Nanoscale* **2013**, *5*, 3283–3288; b) M. Wu, J. Qiao, K. Li, X. Zhou, Y. Liu, J. Zhang, *Green Chem.* **2016**, *18*, 2699–2709; c) G. Zou, H. Hou, G. Zhao, Z. Huang, P. Ge, X. Ji, *Green Chem.* **2017**, *19*, 4622–4632; d) C. Jackson, M. Shahsahebi, T. Wedlake, C. A. Dubard, *Energy Environ. Sci.* **2013**, *6*, 2465–2476; e) S. Wang, D. Zhang, B. Li, C. Zhang, Z. Du, H. Yin, X. Bi, S. Yang, *Adv. Energy Mater.* **2018**, *8*, 1801345.
- [21] I. Shimoyama, T. Hakoda, A. Shimada, Y. Baba, *Carbon* **2015**, *81*, 260–271.
- [22] a) Y. Su, Z. Yao, F. Zhang, H. Wang, Z. Mics, E. Cánovas, M. Bonn, X. Zhuang, X. Feng, *Adv. Funct. Mater.* **2016**, *26*, 5893–5902; b) J. P. Paraknowitsch, Y. Zhang, B. Wienert, A. Thomas, *Chem. Commun.* **2013**, *49*, 1208–1210.
- [23] H. Song, N. Li, H. Cui, C. Wang, *Nano Energy* **2014**, *4*, 81–87.
- [24] L. P. Ding, F. H. Zhang, Y. S. Zhu, C. Lu, X. Y. Kuang, J. Lv, P. Shao, *Sci. Rep.* **2015**, *5*, 15951.
- [25] P. Ge, H. Hou, C. E. Banks, C. W. Foster, S. Li, Y. Zhang, J. He, C. Zhang, X. Ji, *Energy Storage Mater.* **2018**, *12*, 310–323.
- [26] S. J. Blanksby, G. B. Ellison, *Acc. Chem. Res.* **2003**, *36*, 255–263.
- [27] Y. Yan, Y. X. Yin, Y. G. Guo, L. J. Wan, *Adv. Energy Mater.* **2014**, *4*.
- [28] S. Li, J. Qiu, C. Lai, M. Ling, H. Zhao, S. Zhang, *Nano Energy* **2015**, *12*, 224–230.
- [29] H. Lindström, S. Södergren, A. Solbrand, H. Rensmo, J. Hjelm, A. Hagfeldt, S. Lindquist, *J. Phys. Chem. B* **1997**, *101*, 7717–7722.
- [30] a) Y. Yan, Y. X. Yin, S. Xin, Y. G. Guo, L. J. Wan, *Chem. Commun.* **2012**, *48*, 10663–10665; b) G. Yang, H. Song, H. Cui, C. Wang, *J. Mater. Chem. A* **2015**, *3*, 20065–20072.
- [31] W. H. Shin, H. M. Jeong, B. G. Kim, J. K. Kang, J. W. Choi, *Nano Lett.* **2012**, *12*, 2283–2288.
- [32] a) W. Zhou, X. Xiao, M. Cai, L. Yang, *Nano Lett.* **2014**, *14*, 5250–5256; b) H. Yamin, A. Gorenstein, J. Penciner, Y. Sternberg, E. Peled, J. Electrochem. Soc. **1988**, *135*, 1045–1048; c) Y.-S. Su, Y. Fu, T. Cochell, A. Manthiram, *Nat. Commun.* **2013**, *4*, 2985.
- [33] F. Weigend, R. Ahlrichs, *Phys. Chem. Chem. Phys.* **2005**, *7*, 3297–3305.

Manuscript received: February 24, 2019

Revised manuscript received: March 26, 2019

Version of record online: April 10, 2019